Journal of Advanced Ceramics
2017, **6**(2): 100–109
DOI: 10.1007/s40145-017-0222-8

ISSN 2226-4108
CN 10-1154/TQ

Research Article

Magnetoresistivity studies for BiPb-2223 phase added by $BaSnO_3$ nanoparticles

Mai ME. BARAKAT[a,*], Khulud HABANJAR[b]

[a]*Department of Physics*, *Faculty of Science*, *Alexandria University*, *Alexandria*, *Egypt*
[b]*Department of Physics*, *Faculty of Science*, *Beirut Arab University*, *Beirut*, *Lebanon*

Received: December 14, 2016; Revised: February 13, 2017; Accepted: March 17, 2017

Abstract: Co-precipitation method and conventional solid-state reaction technique were used to synthesize $BaSnO_3$ nanoparticles and $(BaSnO_3)_x/Bi_{1.6}Pb_{0.4}Sr_2Ca_2Cu_3O_{10+\delta}$ ($0 \leqslant x \leqslant 1.50$ wt%) samples, respectively. X-ray powder diffraction (XRD), scanning electron microscopy (SEM), and electrical resistivity data were used to characterize BiPb-2223 phase added by $BaSnO_3$ nanoparticles. The relative volume fraction and superconducting transition temperature T_c of BiPb-2223 phase were enhanced by increasing $BaSnO_3$ addition up to 0.50 wt%. These parameters were decreased with further increase of x. The resistive transition broadening under different applied DC magnetic fields (0.29–4.40 kG) was analyzed through thermally activated flux creep (TAFC) model and Ambegaokar–Halperin (AH) theory. Improvements of the derived flux pinning energy U, critical current density $J_c(0)$ estimated from AH parameter $C(B)$, and upper critical magnetic field $B_{c2}(0)$, were recorded by adding $BaSnO_3$ nanoparticles up to 0.50 wt%, beyond which these parameters were suppressed. The magnetic field dependence of the flux pinning energy and critical current density decreased as a power-law relation, which indicated the single junction sensitivity between the superconducting grains to the applied magnetic field. Furthermore, the increase in the applied magnetic field did not affect the electronic thermal conductivity κ_e above the superconducting transition temperature and suppressed it below T_c.

Keywords: BiPb-2223; $BaSnO_3$ nanoparticles; flux pinning energy; critical current density

1 Introduction

Three phases are included in Bi-based superconductors with general formula $Bi_2Sr_2Ca_{n-1}Cu_nO_{2n+4+\delta}$ ($n = 1$, 2, 3). Bi-2223 phase is the most distinguished phase due to its high superconducting transition temperature in the magnitude of 110 K as the number of its atomic CuO_2 planes increases to three [1]. Moreover, it is characterized by higher values of coherence length along c-axis, $\xi_c(0)$, and J_c, which are accompanied by the lower superconducting anisotropy [2]. The partial substitution of Bi^{3+} ions with Pb^{2+} ions significantly enhances the structure stability and promotes the formation of Bi-2223 phase [3], as the presence of Pb at Bi site hinders the additional oxygen atom intersection into Bi–O double layers.

Since the discovery of high temperature superconductors (HTSCs), many technological applications such as HTSC tapes, resonators, wires, tapes, single charge devices, antennas, and switches are achieved. There are many problems facing these

* Corresponding author.
E-mail: maibarakat_phy@yahoo.com

applications, but the crucial limitation is the motion of vortices which creates resistance and causes energy dissipation. Therefore, it is important to pin vortices in order to maintain the nondissipative transport current. The pinning of these vortices can be achieved either by natural pinning centers such as imperfections, defects, and grain boundaries, or by artificial pinning centers represented in the form of chemical doping, neutron irradiation, and heavy ion irradiation [4–6]. The straightforward novel technique to enhance flux pinning is achieved by adding nanoparticles of different weight percentages into HTSC matrix. It was reported that the improvements of both flux pinning and J_c are achieved by the addition of various oxide nanoparticles, such as ZrO_2 [7], Al_2O_3 [8], SnO_2 [9], ZnO [10], Cr_2O_3 [11], and $NiFe_2O_4$ [12], into the selected BiPb-2223 phase.

The resistive transition broadening under applied magnetic field has been discussed by various models such as flux flow [13], TAFC [14], flux cutting, and flux line melting [15] to understand the mechanism of flux motion and flux pinning. Several researchers [16–19] reported that the TAFC model can work well at low temperatures ($U \gg k_B T$) and play a significant role in the resistivity region near T_c to $\rho \approx 0$ ($T_g < T < T_c$), where T_g is the temperature of glass transition that separates the glass vortex ($T < T_g$) and liquid vortex ($T > T_g$) phases. TAFC was first pointed out by Anderson [14], at which creep involves bundles of flux lines hopping over the pinning barriers due to the thermal activation although Lorentz force exerted on the flux bundle by the current is smaller than the pinning force. Several researchers have pointed out that the TAFC model is the best model for describing the electrical resistivity broadening data under applied magnetic field for various phases of Bi-based superconductors [20–28]. Ambegaokar and Halperin's theory is another approach to study the flux line motion under applied magnetic field [29]. This theory describes the thermal fluctuation effect on the phase of the order parameter across a current-driven Josephson junction [30].

In this article, $BaSnO_3$ nanoparticles of different weight percentages were added into BiPb-2223 phase in an attempt to create pinning centers that enhance flux pinning. For such purpose, a series of $(BaSnO_3)_x$/ $Bi_{1.6}Pb_{0.4}Sr_2Ca_2Cu_3O_{10+\delta}$ ($0 \leqslant x \leqslant 1.50$ wt%) samples were prepared by using conventional solid-state reaction technique. The prepared samples were characterized using X-ray powder diffraction (XRD) and electrical resistivity measurements. The resistive transition broadening by decreasing temperature and applying magnetic fields started from 0.29 up to 4.40 kG was analyzed using TAFC model and AH theory. Several superconducting parameters were calculated for BiPb-2223 phase as a function of $BaSnO_3$ nanoparticle addition.

2 Theoretical approach

From TAFC model, broadening of the tail part can be fitted according to Arrhenius relation [31] as

$$\rho(B,T) = \rho_0 \exp[-U(B,T)/(k_B T)] \quad (1)$$

where ρ_0 is the magnetic field and the orientation independent pre-exponential factor. $U(B,T)$ is the flux pinning energy needed to activate the vortex motion, and it gives information about the dissipation mechanism. $U(B,T)$ depends on both magnetic field and temperature. The dependence of $U(B)$ on magnetic field obeys the power-law relation as

$$U(B) \sim B^{-\beta} \quad (2)$$

where β is the magnetic field orientation dependent constant with respect to the basal plane. On the other hand, the dependence of transition width ΔT on magnetic field obeys the power-law relation as

$$\Delta T \sim B^n \quad (3)$$

According to AH theory, the resistivity appears due to weakly coupled grains, and it has the same dependence on energy barrier in the low current limit, which is much less than the maximum Josephson current [13,29] as

$$\rho(T) = \rho_n (I_0 \gamma / 2)^{-2} \quad (4)$$

where ρ_n is the average normal resistivity of the junction, I_0 is the modified Bessel function, and γ is the normalized barrier height [29]:

$$\gamma(B,T) = U(B,T)/(k_B T)$$

From TAFC model and AH theory, $U(B,T)$ can be expressed as [32,33]:

$$U(B,T) \sim \Delta T B^{-\eta}, \quad \eta = \beta + n \quad (5)$$

In AH theory, the physical picture of the normalized barrier height makes the separation of magnetic field effect and thermal effect in the normalized barrier height achieved as

$$\gamma(B,T) = C(B)(1-t)^q \quad (6)$$

where $t = T/T_c$ is the reduced temperature, $q = \beta/n$

[32,33], and $C(B)$ is a magnetic field dependent parameter from which the critical current density at 0 K can be calculated using the following relation [30]:

$$J_c(0) = C(B)ek_B T_c / (\hbar d^2) \quad (7)$$

where d is the average grain size obtained from SEM images. The dependence of $J_c(0)$ on magnetic field obeys the power-law relation as

$$J_c(0) \sim B^{-m} \quad (8)$$

The upper critical magnetic field at 0 K is estimated from the following equation [34]:

$$B_{c2}(0) = 0.69[\mathrm{d}B_{c2}(T)/\mathrm{d}T]T^* \quad (9)$$

where $\mathrm{d}B_{c2}(T)/\mathrm{d}T$ is the slope obtained from $B_{c2}(T)$ versus T plot at the highest value of the applied magnetic field, and T^* is the tangent intersection with the temperature axis. Moreover, the coherence length along weak links at 0 K could be determined from the following expression [21] as

$$\xi(0) = \sqrt{\phi_0/[2\pi B_{c2}(0)]} \quad (10)$$

where ϕ_0 is the magnetic flux quantum.

The phonon thermal conductivity contribution κ_{ph} due to lattice vibration and electronic thermal contribution κ_e are the two responsible contributions for the thermal conductivity in HTSCs. The electronic thermal contribution can be expressed through Wiedermann–Franz law [35] as

$$\kappa_e = \pi^2 k_B^2 T / (3e^2 \rho) \quad (11)$$

3 Experimental details

$BaSnO_3$ nanoparticles were prepared by co-precipitation method. Stoichiometric amounts of pure chemical reagents $BaCl_2{\cdot}2H_2O$ and $SnCl_4{\cdot}5H_2O$ were dissolved in distilled water to prepare aqueous solutions by using NaOH as a buffer. $BaCl_2{\cdot}2H_2O$ solution was heated up to 75 ℃, then NaOH was added dropwise till pH increased to 13. Once the required pH was reached, $SnCl_4{\cdot}5H_2O$ solution was slowly added. Simultaneous heating with continuous stirring at 95 ℃ for 1 h was done. The white precipitated powders were washed repeatedly with distilled water till all chlorine got removed and pH = 7, and dried at 100 ℃ for 24 h. The dried powders were finally calcined at 900 ℃ for 2 h.

Conventional solid-state reaction technique was used to synthesize $(BaSnO_3)_x$/BiPb-2223 ($0 \leqslant x \leqslant 1.50$ wt% samples. High-purity (99.99%, Aldrich Chem. Co.) of Bi_2O_3, PbO, $SrCO_3$, CaO, and CuO powders were well ground, mixed, sifted, and calcinated in air at 820 ℃ for 24 h. This process was repeated twice after intermediate grinding and sieving. $BaSnO_3$ nanoparticles of different weight percentages were added to the resultant powders. The powders were mixed, grounded, sifted, and finally pressed into pellets using a hydraulic press under 15 ton/cm^2 pressure to decrease the number of voids and minimize the intergrain contact problems. Pellets (1.5 cm in diameter and 0.3 cm in thickness) were sintered in air at 845 ℃ with a heating rate of 4 ℃/min and held at this temperature for 96 h. The samples were finally cooled down by a rate of 2 ℃/min to room temperature.

Philips X'pert X-ray diffractometer with Cu Kα radiation (λ = 1.54056 Å) was used to measure XRD of all the prepared samples. The samples' surface morphology was examined using a Jeol SEM, JSM-5300, operated at 25 kV with a resolution power of 1 μm. A closed cryogenic refrigeration system measured the samples' electrical resistivity from room temperature down to zero resistivity temperature. A chromel versus Fe–Au thermocouple monitored the temperature of the samples, which stabilized within ±0.1 K through a temperature controller. The electrical resistivity versus temperature was measured under different applied DC magnetic fields of 0.29, 0.50, 1.20, 2.34, 3.53, and 4.40 kG. DC electromagnet was used to generate the magnetic field, which was applied normally to the direction of the driving current.

4 Results and discussion

Figure 1 shows the XRD pattern of $BaSnO_3$ nanoparticles. All peaks are indexed by a cubic structure with a space group *Pm*3*m*, indicating the high

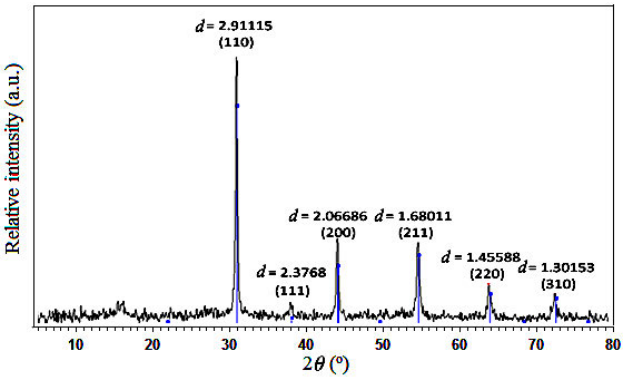

Fig. 1 XRD pattern for $BaSnO_3$ nanoparticles.

purity of the prepared $BaSnO_3$ nanoparticles. The calculated lattice parameters are $a=b=c=4.119$ Å. Similar XRD peaks of $BaSnO_3$ with an average lattice parameter in the magnitude of 4.108 Å were reported by Sahoo *et al.* [36]. The average crystalline size of $BaSnO_3$ nanoparticles is 34.8 nm, calculated using Williamson–Hall plot relation [37].

Figure 2 displays XRD patterns for $(BaSnO_3)_x$/BiPb-2223 ($0 \leqslant x \leqslant 1.50$ wt%) samples. All major XRD peaks are indexed by a tetragonal unit cell with a space group *P*4/*mmm*, except minor peaks which belong to BiPb-2212 and Ca_2PbO_4 phases. The peaks of BiPb-2223 and BiPb-2212 phases are indicated by (*hkl*)H and (*hkl*)L, respectively. It is obvious that peak positions do not change and no additional secondary phases are appeared by increasing the addition of $BaSnO_3$ nanoparticles into BiPb-2223 phase. Therefore, the addition of $BaSnO_3$ nanoparticles does not result in the appearance of any $BaSnO_3$-rich compounds. Also, there is not any change in the position of the peaks, indicating that $BaSnO_3$ nanoparticles do not enter the lattice. Similar results of unchanged peak positions and undetected nanoparticle-rich phases were obtained by adding ZrO_2 [7], Al_2O_3 [8], and SnO_2 [9,38] nanoparticles into BiPb-2223 phase. The relative volume fraction values of BiPb-2223, BiPb-2212, and Ca_2PbO_4 phases are calculated from the following equations, respectively, and listed in Table 1 versus $BaSnO_3$ nanoparticle addition.

$$\text{BiPb-2223}(\%) = \frac{I_{\text{BiPb-2223}}}{I_{\text{BiPb-2223}} + I_{\text{BiPb-2212}} + I_{\text{Ca}_2\text{PbO}_4}} \times 100\% \quad (12)$$

$$\text{BiPb-2212}(\%) = \frac{I_{\text{BiPb-2212}}}{I_{\text{BiPb-2223}} + I_{\text{BiPb-2212}} + I_{\text{Ca}_2\text{PbO}_4}} \times 100\% \quad (13)$$

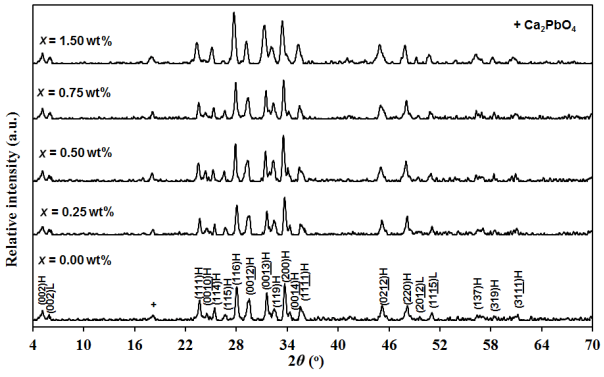

Fig. 2 XRD patterns for $(BaSnO_3)_x$/BiPb-2223 ($0 \leqslant x \leqslant 1.50$ wt%) samples.

$$\text{Ca}_2\text{PbO}_4(\%) = \frac{I_{\text{Ca}_2\text{PbO}_4}}{I_{\text{BiPb-2223}} + I_{\text{BiPb-2212}} + I_{\text{Ca}_2\text{PbO}_4}} \times 100\% \quad (14)$$

where I is the phase peak intensity. The addition of $BaSnO_3$ nanoparticles up to 0.50 wt% enhances the relative volume fraction of BiPb-2223 phase, beyond which it is decreased. Variation of relative volume fraction for BiPb-2212 phase versus x has a reverse trend. The enhancement of the relative volume fraction for BiPb-2223 phase could be explained due to the addition of $BaSnO_3$ nanoparticles up to 0.50 wt%. Such addition is crucial in affecting the viscosity of the transient liquid formed at the reaction temperature, its homogeneity, and the formation rate of the BiPb-2223 phase [8]. However, its decrease with $x \geqslant 0.75$ wt% could be due to the ability of solid $BaSnO_3$ nanoparticles to prevent the spatial growth of BiPb-2223 phase. Similar behavior of the relative volume fraction for BiPb-2223 phase was obtained with the addition of different nanoparticles [9,11,38]. The lattice parameters a and c, calculated by using the least-squares method, are listed in Table 1 versus $BaSnO_3$ nanoparticle addition. There is almost no change in the values of a and c by increasing the addition of $BaSnO_3$ nanoparticles, confirming that $BaSnO_3$ nanoparticles do not enter the crystal structure of BiPb-2223 phase. This means that $BaSnO_3$ acts only at the grain boundaries. Similar results were reported by Yavuz *et al.* [38] for BiPb-2223 phase added by SnO_2 nanoparticles.

Figures 3(a) and 3(b) display SEM images for $(BaSnO_3)_x$/BiPb-2223 samples with $x=0$ and 1.50 wt%, respectively. The distribution of the random alignment platelet-like grains is a signature for the formation of BiPb-2223 phase. Evidently, the appearance of white dots in Fig. 3(b) indicates the distribution of $BaSnO_3$ nanoparticles throughout the intergrain region. This reveals that $BaSnO_3$ nanoparticles occupy the interstitial positions between

Table 1 Variation of relative volume fraction of BiPb-2223, BiPb-2212, and Ca_2PbO_4 phases, lattice parameters, T_c, and P for $(BaSnO_3)_x$/BiPb-2223 samples

x (wt%)	BiPb-2223 (%)	BiPb-2212 (%)	Ca_2PbO_4 (%)	a (Å)	c (Å)	T_c (K)	P
0.00	93.4	5.5	1.1	5.394(1)	37.18(8)	104.75	0.136
0.25	94.6	4.3	1.1	5.392(9)	37.20(4)	106.00	0.139
0.50	95.0	3.5	1.5	5.394(2)	37.21(2)	107.25	0.143
0.75	92.0	6.7	1.3	5.392(6)	37.22(8)	103.50	0.133
1.50	89.1	9.4	1.5	5.395(7)	37.26(8)	101.00	0.129

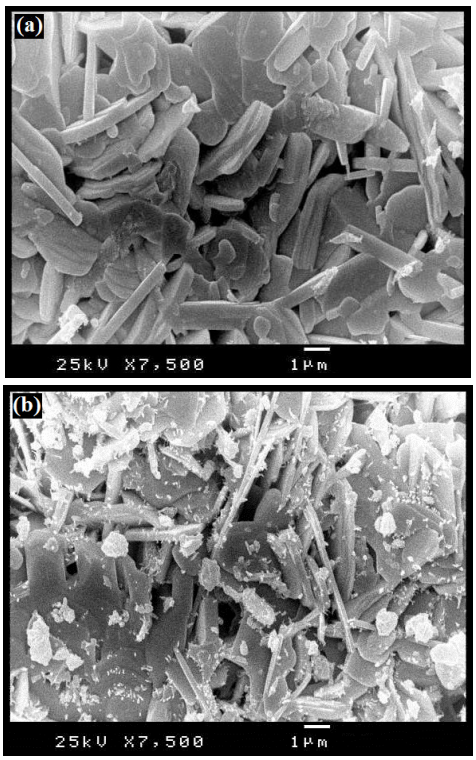

Fig. 3 SEM micrographs for (a) BiPb-2223 sample and (b) $(BaSnO_3)_{1.5wt\%}$/BiPb-2223 sample.

grains, confirming the results obtained from XRD data. Similar observation was detected for BiPb-2223 phase added by SnO_2 [38], Cr_2O_3 [39], and $NiFe_2O_4$ [12] nanoparticles.

Figure 4 shows the electrical resistivity behavior versus temperature for $(BaSnO_3)_x$/BiPb-2223 ($0 \leqslant x \leqslant 1.50$ wt%) samples. A normal state metallic-like behavior is observed by decreasing T, followed by a nearly sharp superconducting transition. Normal state electrical resistivity is increased by increasing the addition of $BaSnO_3$ nanoparticles into BiPb-2223 phase, which reflects the improvement of the scattering mechanism or nanoparticle random distributions at grain boundaries. The calculated T_c, recorded as the maximum point of $d\rho/dT$ versus T plot, is listed in Table 1 versus x. T_c is improved by increasing x up to 0.50 wt%, beyond which T_c is decreased. This enhancement in T_c is a result of the improvement in relative volume fraction, intergrain connectivity, or/and the change in oxygen content by adding $BaSnO_3$ nanoparticles. Similar enhancement in both T_c and relative volume fraction was obtained by adding SnO_2 [9], Cr_2O_3 [11], and $NiFe_2O_4$ [12] nanoparticles into BiPb-2223 phase. Furthermore, the decrement in T_c is

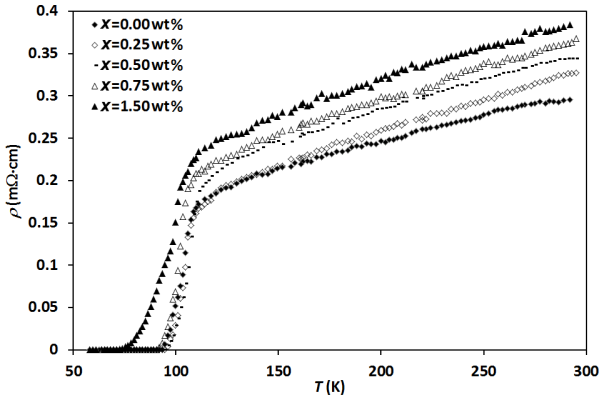

Fig. 4 Plots of electrical resistivity versus temperature for $(BaSnO_3)_x$/BiPb-2223 samples.

attributed to the suppression of relative volume fraction for BiPb-2223 phase or mobile carrier trapping as a result of oxygen vacancy disorder [40]. The hole carrier concentration per Cu ion P can be calculated through the following equation [41] as

$$P = 0.16 - \left[\left(1 - \frac{T_c}{T_c^{max}}\right)/82.6\right]^{0.5} \quad (15)$$

where T_c^{max} is taken as 110 K for BiPb-2223 phase. The values of P with x are also listed in Table 1, and have the same trend behavior of T_c versus x. Similar behavior of P with x was obtained for $(SnO_2)_x$/BiPb-2223 samples [38].

For all HTSCs, Gaussian fluctuation theory can analyze the superconducting fluctuation effects just above T_c. In the absence of magnetic field, the broadening of the resistive transition is attributed to the weak coupling superconducting grains [42]. Variation of $\ln(\rho)$ versus $1/T$ under applied magnetic fields ranged from 0.29 to 4.40 kG is displayed in Figs. 5 and 6 for $(BaSnO_3)_x$/BiPb-2223 samples with $x = 0$ and 1.50 wt%, respectively. In presence of magnetic field, the resistive transition is characterized by two sections, which are the main steep or pairing transition part and broadening tail part. The pairing transition part is almost unchanged as there is no motion for vortices near the superconducting transition temperature, reflecting a strong intragrain pinning energy. The broadening tail part ($T_g < T < T_c$) is extremely sensitive to the applied magnetic field even for small values and shifts to lower temperatures by increasing the applied magnetic field, as the flux penetrates inside the superconducting grains. This broadening is proportional to the magnitude and strength of pinning force. TAFC model and AH theory

are usually used to analyze this broadening. At the glass vortex phase $T < T_g$, the disorder dominates and the linear resistance is zero at lower temperatures in the limit of very small current. The glass transition temperature can be determined from the linear extrapolation to zero of $(\mathrm{d}\ln(\rho)/\mathrm{d}T)^{-1}$ versus T plot [7]. The insets of Figs. 5 and 6 show the variation of T_g versus B. T_g shifts to lower values by increasing the applied magnetic field. Comparable shift was reported by Zouaoui *et al.* [7] for $(ZrO_2)_x$/BiPb-2223 samples. To eliminate the temperature dependence of the flux pinning energy and by using Eq. (1), the values of $U(B)$ can be directly calculated from the slope of each linear part multiplied by Boltzmann's constant k_B as depicted in Figs. 5 and 6. The relation between $U(B)$ versus the applied magnetic field is displayed in Fig. 7. $U(B)$ is decreased rapidly by increasing the applied magnetic field up to 1.20 kG, beyond which a slight decrease as plateau is observed. The increase in the applied magnetic field in the intergranular space destructs the weak link network, causing a rapid decrease in $U(B)$. For $B \geqslant 2.34$ kG, the flux from the external magnetic field penetrates the grain bulk, and it is trapped there leaving the intergranular field almost unchanged [43]. Complementary trend was observed for BiPb-2223 phase added by Mn [28] and $MgCO_3$ [44]. Moreover, $U(B)$ is increased by increasing the addition of $BaSnO_3$ nanoparticles up to 0.50 wt%, confirming the behavior of T_c and calculated relative volume fraction versus $BaSnO_3$ nanoparticle addition. Similar enhancement in $U(B)$ accompanied by an increase in both T_c and the relative volume fraction was reported by Abbasi *et al.* [11] for $(Cr_2O_3)_x$/BiPb-2223 samples. For $x \geqslant$ 0.75 wt%, the vortices creep more easily as the weak links are increased, whereas $U(B)$ is decreased [45]. Using Eq. (2), the obtained values of β versus x are listed in Table 2. The values of β for $(BaSnO_3)_x$/BiPb-2223 samples are close to those obtained for BiPb-2223 phase substituted by Ru^{4+} ions ($\beta = 0.25$–0.36) [27], and in contrary with those obtained for $(Mn)_x$/BiPb-2223 samples ($\beta = 0.45$–0.61) [28]. Consequently, there are no expectation values of β as they depend on many factors affected on the pinning energy to the characteristics of crystal structure such as the atoms' real position, weak link quality, and oxygen content [45]. To overcome the magnetic field dependence of flux pinning energy, $U(T)$ is determined by plotting relation between ΔT and B as depicted in Fig. 8 for $(BaSnO_3)_x$/BiPb-2223 samples. The increase in ΔT by increasing B can be discussed as a number of randomly orientated grains will freeze and cluster in random positions under cooling. Accordingly, this leads to a more resistive state of all samples, which weaken the vortex pinning strength due to the loss of complete

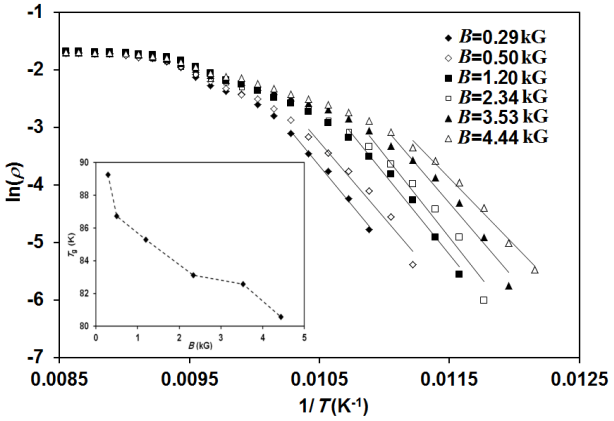

Fig. 5 $\ln(\rho)$ versus $1/T$ plots for BiPb-2223 sample. The inset shows the applied magnetic field dependence of T_g.

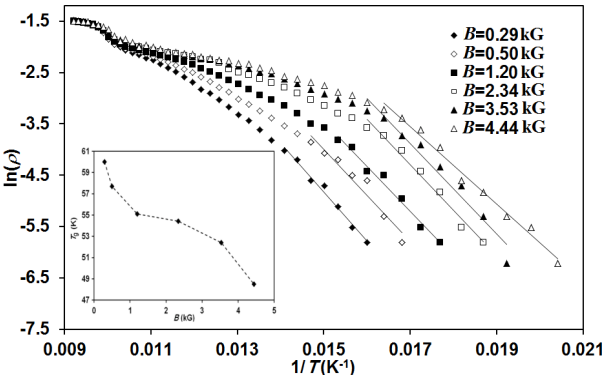

Fig. 6 $\ln(\rho)$ versus $1/T$ plots for $(BaSnO_3)_{1.5wt\%}$/BiPb-2223 sample. The inset shows the applied magnetic field dependence of T_g.

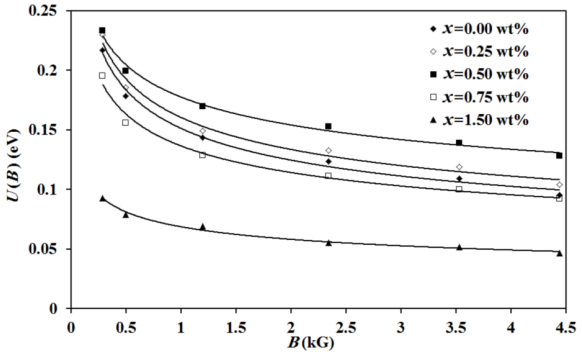

Fig. 7 Relation between $U(B)$ and B for $(BaSnO_3)_x$/BiPb-2223 samples.

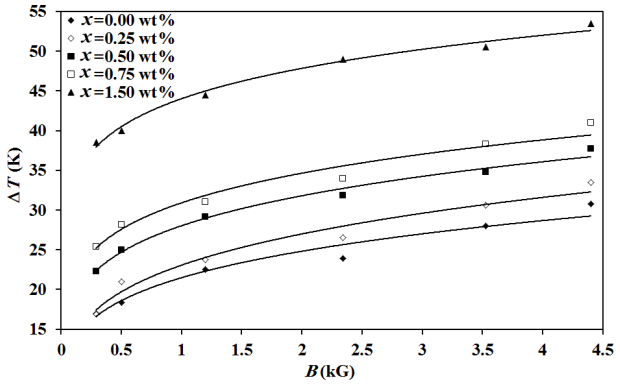

Fig. 8 Relation between transition width and applied magnetic field for $(BaSnO_3)_x$/BiPb-2223 samples.

superconducting current paths [46]. The increase in ΔT by increasing the addition $BaSnO_3$ nanoparticles could be due to the increase in microscopic inhomogeneities (nonsuperconducting phases) and/or weaken of intergrain connectivity. The values of n obtained by using Eq. (3), in addition to the parameters η and q, are also listed in Table 2 versus x.

Using AH parameter $C(B)$, $J_c(0)$ can be determined from Eq. (7) and its behavior versus B is displayed in Fig. 9. Obviously, $J_c(0)$ is decreased by increasing B, indicating the sensitive dependence of applied magnetic field on the single junction between the superconducting grains. Using Eq. (8), the relation of the critical current density versus x is depicted in the inset of Fig. 9. The addition of $BaSnO_3$ nanoparticles up to 0.50 wt% into BiPb-2223 phase improves the critical current density. This reflects the probability of creating pinning centers or generating locally weak superconducting regions that enrich the flux pinning by adding $BaSnO_3$ nanoparticles. Moreover, the suppression in $J_c(0)$ with $x \geqslant 0.75$ wt% could be interpreted due to the increase in grain boundary resistance or nonsuperconducting impurities.

Table 2 Variation of β, n, η, and q versus x for $(BaSnO_3)_x$/BiPb-2223 samples

x (wt%)	β	n	η	q
0.00	0.258	0.227	0.485	1.137
0.25	0.234	0.205	0.439	1.140
0.50	0.226	0.185	0.411	1.220
0.75	0.250	0.175	0.425	1.431
1.50	0.244	0.140	0.384	1.740

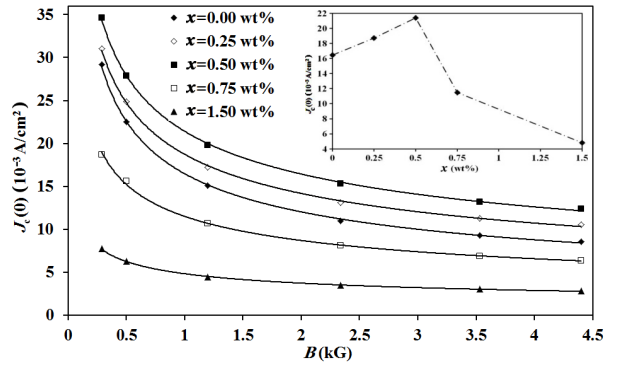

Fig. 9 Relation between critical current density at 0 K and B for $(BaSnO_3)_x$/BiPb-2223 samples. The inset shows relation between $J_c(0)$ versus x.

By considering 10% of normal state resistivity in T_c measurements, the upper critical magnetic field can be calculated. The plots of $B_{c2}(T)$ versus T for $(BaSnO_3)_x$/BiPb-2223 samples is displayed in Fig. 10. A gradual change in $B_{c2}(T)$ near T_c by decreasing temperature, followed by a rapid increase with a strong positive curvature at lower temperatures is observed. Using Eqs. (9) and (10), the variation of $B_{c2}(0)$ and $\xi(0)$ with x is depicted in Fig. 11. $B_{c2}(0)$ is enhanced by increasing the addition of $BaSnO_3$ nanoparticles up to 0.50 wt%, beyond which it is decreased. A reverse trend of variation for $\xi(0)$ versus x is observed.

From Eq. (11), the variation of calculated κ_e versus T under applied magnetic field is depicted in Fig. 12 for $(BaSnO_3)_{0.75wt\%}$/BiPb-2223 sample. Noticeably, κ_e is

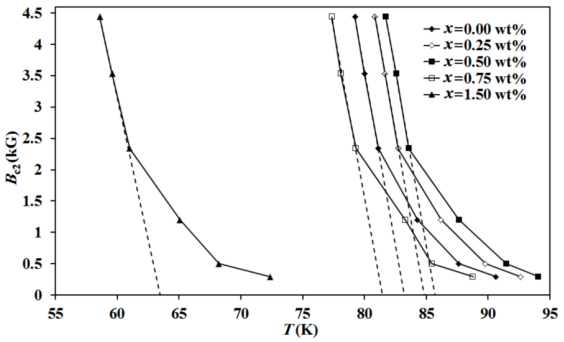

Fig. 10 Plots of $B_{c2}(T)$ versus T for $(BaSnO_3)_x$/BiPb-2223 samples.

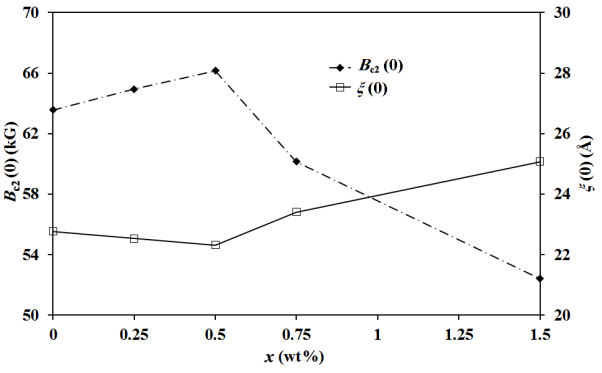

Fig. 11 Variation of $B_{c2}(0)$ and $\xi(0)$ versus x for $(BaSnO_3)_x$/BiPb-2223 samples.

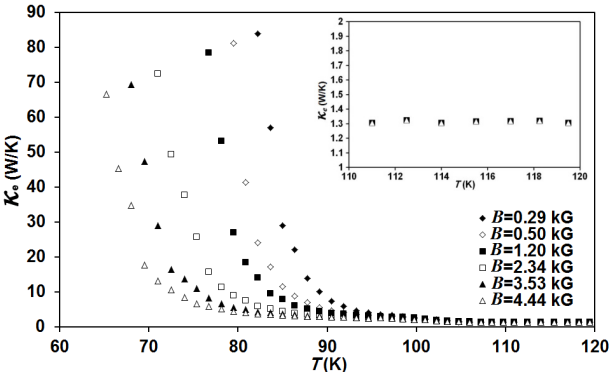

Fig. 12 Relation between κ_e versus T under applied magnetic field for $(BaSnO_3)_{0.75wt\%}$/BiPb-2223 sample. The inset shows magnetic field independence of κ_e with T.

decreased rapidly by increasing temperature up to T_c due to electrons' disability to transfer heat as they are condensed into Cooper pairs [47], followed by a near temperature independent behavior as plateau as displayed in the inset of Fig. 12 by further increase in T. However, the suppression in the electronic thermal conductivity by increasing B below the superconducting transition temperature is probably due to the additional scattering centers of vortices [48]. Above the superconducting transition temperature, κ_e is magnetic field independent [33].

5 Conclusions

Series of $(BaSnO_3)_x$/BiPb-2223 samples were synthesized using conventional solid-state reaction technique. The crystal structure of BiPb-2223 phase was not impacted by adding $BaSnO_3$ nanoparticles as they occupied the intergrain position. The relative volume fraction, T_c, and P were improved by increasing x up to 0.50 wt%. Magnetoresistivity data was analyzed using TAFC model and AH theory. The enhancement of the derived flux pinning energy, the critical current density, and $B_{c2}(0)$ by increasing x up to 0.50 wt% were also reported. A reverse trend was observed by further increase in x. The little addition of $BaSnO_3$ nanoparticles might create pinning centers or probably generate locally weak superconducting regions into BiPb-2223 phase, which enhanced the superconducting magnetic parameters. On the contrary, the formation of weak links into BiPb-2223 phase might be obtained for high $BaSnO_3$ nanoparticle addition. The electronic thermal conductivity was decreased by increasing the applied magnetic field below T_c.

Acknowledgements

Many thanks are directed to Prof. Dr. A. I. Abou-Aly, the leader of Superconductivity and Metallic Glasses Group Lab where this work was done, as well as Prof. Dr. R. Awad and Prof. Dr. N. H. Mohammed for their support to this work.

References

[1] Sarkar AK, Maartense I, Peterson TL, *et al*. Preparation and characterization of superconducting phases in the Bi(Pb)–Sr–Ca–Cu–O system. *J Appl Phys* 1989, **66**: 3717.

[2] Blatter G, Feigel'man MV, Ceshkenbein VB, *et al*. Vortices in high-temperature superconductors. *Rev Mod Phys* 1994, **66**: 1125.

[3] Upadhyay PL, Rao SUM, Nagpal KC, *et al*. Microstructures and the role of Pb in doped Bisrcacuo superconductor. *Mater Res Bull* 1992, **27**: 109–116.

[4] Trastoy J, Rouco V, Ulysse C, *et al*. Nanostructuring of high-T_C superconductors via masked ion irradiation for efficient ordered vortex pinning. *Physica C* 2014, **506**: 195–200.

[5] Shahbazi M, Wang XL, Ghorbani SR, *et al*. Vortex-glass phase transition and enhanced flux pinning in C^{4+}-irradiated $BaFe_{1.9}Ni_{0.1}As_2$ superconducting single crystals. *Supercond Sci Tech* 2013, **26**: 095014.

[6] Eisterer M, Zehetmayer M, Weber HW, *et al*. Effects of disorder on the superconducting properties of $BaFe_{1.8}Co_{0.2}As_2$ single crystals. *Supercond Sci Tech* 2009, **22**: 095011.

[7] Zouaoui M, Ghattas A, Annabi M, *et al*. Effect of nano-size ZrO_2 addition on the flux pinning properties of (Bi,Pb)-2223 superconductor. *Supercond Sci Tech* 2008, **21**: 125005.

[8] Annabi M, M'chirgui A, Azzouz FB, *et al*. Addition of nanometer Al_2O_3 during the final processing of (Bi,Pb)-2223 superconductors. *Physica C* 2004, **405**: 25–33.

[9] Abou-Aly AI, Abdel Gawad MMH, Awad R, *et al*. Improving the physical properties of (Bi,Pb)-2223 phase by SnO_2 nano-particles addition. *J Supercond Nov Magn* 2011, **24**: 2077.

[10] Agail A, Abd-Shukor R. Transport current density of $(Bi_{1.6}Pb_{0.4})Sr_2Ca_2Cu_3O_{10}$ superconductor added with different nano-sized ZnO. *Appl Phys A* 2013, **112**: 501–506.

[11] Abbasi H, Taghipour J, Sedghi H. Superconducting and transport properties of (Bi–Pb)–Sr–Ca–Cu–O with Cr_2O_3 additions. *J Alloys Compd* 2010, **494**: 305–308.

[12] Kong W, Abd-Shukor R. Enhanced electrical transport properties of nano $NiFe_2O_4$-added $(Bi_{1.6}Pb_{0.4})$

$Sr_2Ca_2Cu_3O_{10}$ superconductor. *J Supercond Nov Magn* 2010, **23**: 257.

[13] Tinkham M. Resistive transition of high-temperature superconductors. *Phys Rev Lett* 1988, **61**: 1658.

[14] Anderson PW. Theory of flux creep in hard superconductors. *Phys Rev Lett* 1962, **9**: 309.

[15] Mohammadizadeh MR, Akvahan M. Magnetoresistance in $Gd(Ba_{2-x}Pr_x)Cu_3O_{7+\delta}$ system. *Physica C* 2003, **390**: 134–142.

[16] Palstra TTM, Batlogg B, van Dover RB, *et al*. Critical currents and thermally activated flux motion in high-temperature superconductors. *Appl Phys Lett* 1989, **54**: 763.

[17] Palstra TTM, Batlogg B, Schneemeyer LF, *et al*. Thermally activated dissipation in $Bi_{2.2}Sr_2Ca_{0.8}Cu_2O_{8+\delta}$. *Phys Rev Lett* 1988, **61**: 1662.

[18] Malozemoff AP, Worthington TK, Zeldov E, *et al*. Flux creep and the crossover to flux flow in the resistivity of high-T_c superconductors. In *Strong Correlation and Superconductivity*. Fukuyama H, Maekawa S, Malozemoff AP, Eds. Springer-Verlag Berlin Heidelberg, 1989: 349–360.

[19] Griessen R. Resistive behavior of high-T_c superconductors: Influence of a distribution of activation energies. *Phys Rev Lett* 1990, **64**: 1674.

[20] Yazici D, Erdem M, Ozcelik B. Effect of high valancy cations on the intergranular pinning energies of $(Bi–Pb)_2Sr_2Ca_2Cu_3O_{10+\delta}$ samples. *J Supercond Nov Magn* 2012, **25**: 1811.

[21] Gündoğmuş H, Özçelik B, Sotelo A, *et al*. Effect of Yb-substitution on thermally activated flux creep in the $Bi_2Sr_2Ca_1Cu_{2-x}Yb_xO_y$ superconductors. *J Mater Sci: Mater El* 2013, **24**: 2568–2575.

[22] Özçelik B, Gündoğmuş H, Yazici D. Effect of (Ta/Nb) co-doping on the magnetoresistivity and flux pinning energy of the BPSCCO superconductors. *J Mater Sci: Mater El* 2014, **25**: 2456–2462.

[23] Özkurt B, Özçelik B. Effect of Nd-substitution on thermally activated flux creep in the $Bi_{1.7}Pb_{0.3-x}Nd_xSr_2Ca_3Cu_4O_{12+y}$ superconductors. *J Low Temp Phys* 2009, **156**: 22–29.

[24] Özçelik B, Gürsul M, Sotelo A, *et al*. Improvement of the intergranular pinning energy in the Na-doped Bi-2212 superconductors. *J Mater Sci: Mater El* 2015, **26**: 2830–2837.

[25] Özçelik B, Kaya C, Gündoğmuş H, *et al*. Effect of Ce substitution on the magnetoresistivity and flux pinning energy of the $Bi_2Sr_2Ca_{1-x}Ce_xCu_2O_{8+\delta}$ superconductors. *J Low Temp Phys* 2014, **174**: 136–147.

[26] Özçelik B, Yalaz E, Yakıncı ME, *et al*. The effect of K substitution on magnetoresistivity and activation energy of Bi-2212 system. *J Supercond Nov Magn* 2015, **28**: 553–559.

[27] Abou-Aly AI, Mahmoud SA, Awad R, *et al*. Electrical resistivity and magnetoresistance studies of (Bi,Pb)-2223 phase substituted by Ru. *J Supercond Nov Magn* 2010, **23**: 1575–1588.

[28] Dogruer M, Zalaoglu Y, Varilci A, *et al*. A study on magnetoresistivity, activation energy, irreversibility and upper critical field of slightly Mn added Bi-2223 superconductor ceramics. *J Supercond Nov Magn* 2012, **25**: 961–968.

[29] Ambegaokar V, Halperin BI. Voltage due to thermal noise in the dc Josephson effect. *Phys Rev Lett* 1969, **22**: 1364.

[30] Gamchi HS, Russel GJ, Taylor KNR. Resistive transition for $YBa_2Cu_3O_{7-\delta}–Y_2BaCuO_5$ composites: Influence of a magnetic field. *Phys Rev B* 1994, **50**: 12950.

[31] Palstra TTM, Batlogg B, van Dover RB, *et al*. Dissipative flux motion in high-temperature superconductors. *Phys Rev B* 1990, **41**: 6621.

[32] Khosroabadi H, Daadmehr V, Akhavan M. Magnetic transport properties and Hall effect in $Gd_{1-x}Pr_xBa_2Cu_3O_{7-\delta}$ system. *Physica C* 2003, **384**: 169–177.

[33] Mohammed NH, Abou-Aly AI, Awad R, *et al*. Magnetoresistance studies of Tl-1212 phase substituted by scandium. *Supercond Sci Tech* 2006, **19**: 1104.

[34] Moodera JS, Meservey R, Tkaczyk JE, *et al*. Critical-magnetic-field anisotropy in single-crystal $YBa_2Cu_3O_7$. *Phys Rev B* 1988, **37**: 619.

[35] Kittel C. *Introduction to Solid State Physics*, 8th edn. Wiely, 2004: 156.

[36] Sahoo M, Giri D, Behera D. Study of structural modification and fluctuation induced electrical conductivity in $YBa_2Cu_3O_{7-y}+xBaSnO_3$ sperconductor composite. *J Low Temp Phys* 2014, **177**: 257–273.

[37] Elokr MM, Awad R, El-Ghany AA, *et al*. Effect of nano-sized ZnO on the physical properties of $(Cu_{0.5}Tl_{0.25}Pb_{0.25})Ba_2Ca_2Cu_3O_{10-\delta}$. *J Supercond Nov Magn* 2011, **24**: 1345–1352.

[38] Yavuz Ş, Bilgili Ö, Kocabaş K. Effects of superconducting parameters of SnO_2 nanoparticles addition on (Bi,Pb)-2223 phase. *J Mater Sci: Mater El* 2016, **27**: 4526–4533.

[39] Wei K, Abd-Shukor R. Superconducting and transport properties of (Bi–Pb)–Sr–Ca–Cu–O with nano-Cr_2O_3 additions. *J Electron Mater* 2007, **36**: 1648–1651.

[40] Mellekh A, Zouaoui M, Azzouz FB, *et al*. Nano-Al_2O_3 particle addition effects on Y $Ba_2Cu_3O_y$ superconducting properties. *Solid State Commun* 2006, **140**: 318–323.

[41] Persland MR, Tallon JL, Buckley RG, *et al*. General trends in oxygen stoichiometry effects on T_c in Bi and Tl superconductors. *Physica C* 1991, **176**: 95–105.

[42] Jurelo AR, Kunzler JV, Schaf J, *et al*. Fluctuation conductivity and microscopic granularity in Bi-based high-temperature superconductors. *Phys Rev B* 1997, **56**: 14815.

[43] Abou-Aly AI, Mahmoud SA, Awad R, *et al*. Magnetic transport properties in $GdBa_2Cu_{3-x}Ru_xO_{7-\delta}$ superconducting phase. *J Low Temp Phys* 2012, **167**: 59–73.

[44] Abbasi H, Taghipour J, Sedghi H. The effect of $MgCO_3$ addition on the superconducting properties of Bi2223 superconductors. *J Alloys Compd* 2009, **482**: 552–555.

[45] Mohammadizadeh MR, Akhavan M. Thermally activated flux creep in the $Gd(Ba_{2-x}Pr_x)Cu_3O_{7+\delta}$ system. *Supercond Sci Tech* 2003, **16**: 538.

[46] Abou-Aly AI, Korayem MT, Gomaa NG, *et al*. Synthesis and study of the ceramic high-T_c superconductor $Hg_{1-x}Tl_xBa_2Ca_{1.8}Y_{0.2}Cu_3O_{8+\delta}$ ($x = 0.3$, 0.5, 0.7, 0.9 and 1). *Supercond Sci Tech* 1999, **12**: 147.
[47] Heremans J, Morelli DT, Smith GW, *et al*. Thermal and electronic properties of rare-earth $Ba_2Cu_3O_x$ superconductors. *Phys Rev B* 1988, **37**: 1604.
[48] Uhe C. Thermal conductivity of high-T_c superconductors. *J Supercond* 1990, **3**: 337–389.